



HAL
open science

X-ray nanotomography using near-field ptychography

Marco Stockmar, Maxime Hubert, Martin Dierolf, Bjoern Enders, Richard Clare, Sebastian Allner, Andreas Fehringer, Irene Zanette, Julie Villanova, Jerome Laurencin, et al.

► **To cite this version:**

Marco Stockmar, Maxime Hubert, Martin Dierolf, Bjoern Enders, Richard Clare, et al.. X-ray nanotomography using near-field ptychography. *Optics Express*, 2015, 23 (10), pp.12720-12731. 10.1364/OE.23.012720 . hal-01572817

HAL Id: hal-01572817

<https://hal.science/hal-01572817>

Submitted on 8 Aug 2017

HAL is a multi-disciplinary open access archive for the deposit and dissemination of scientific research documents, whether they are published or not. The documents may come from teaching and research institutions in France or abroad, or from public or private research centers.

L'archive ouverte pluridisciplinaire **HAL**, est destinée au dépôt et à la diffusion de documents scientifiques de niveau recherche, publiés ou non, émanant des établissements d'enseignement et de recherche français ou étrangers, des laboratoires publics ou privés.

X-ray nanotomography using near-field ptychography

Marco Stockmar,^{1,*} Maxime Hubert,^{2,3} Martin Dierolf,¹
Bjoern Enders,¹ Richard Clare,¹ Sebastian Allner,¹
Andreas Fehringer,¹ Irene Zanette,^{1,4}
Julie Villanova,² Jérôme Laurencin,³ Peter Cloetens,²
Franz Pfeiffer,^{1,5} and Pierre Thibault⁶

¹*Lehrstuhl für Biomedizinische Physik, Physik-Department & Institut für Medizintechnik,
Technische Universität München, 85748 Garching, Germany*

²*European Synchrotron Radiation Facility (ESRF), 71 avenue des Martyrs, 38000 Grenoble,
France*

³*Univ. Grenoble Alpes - CEA, LITEN, 17 rue des Martyrs, 38054, Grenoble, France*

⁴*Current address: Diamond Light Source, Harwell Science and Innovation Campus,
Didcot, OX11 0DE, United Kingdom*

⁵*Institut für diagnostische und interventionelle Radiologie, Klinikum rechts der Isar,
Technische Universität München, 81675 München, Germany*

⁶*Department of Physics & Astronomy, University College London, London, United Kingdom*

[*marco.stockmar@ph.tum.de](mailto:marco.stockmar@ph.tum.de)

Abstract: Propagation-based imaging or inline holography in combination with computed tomography (holotomography) is a versatile tool to access a sample's three-dimensional (3D) micro or nano structure. However, the phase retrieval step needed prior to tomographic reconstruction can be challenging especially for strongly absorbing and refracting samples. Near-field ptychography is a recently developed phase imaging method that has been proven to overcome this hurdle in projection data. In this work we extend near-field ptychography to three dimensions and we show that, in combination with tomography, it can access the nano structure of a solid oxide fuel cell (SOFC). The quality of the resulting tomographic data and the structural properties of the anode extracted from this volume were compared to previous results obtained with holotomography. This work highlights the potential of 3D near-field ptychography for reliable and detailed investigations of samples at the nanometer scale, with important applications in materials and life sciences among others.

© 2015 Optical Society of America

OCIS codes: (100.5070) Phase retrieval; (180.7460) X-ray microscopy; (110.6960) Tomography.

References and links

1. M. Dierolf, A. Menzel, P. Thibault, P. Schneider, C. M. Kewish, R. Wepf, O. Bunk, and F. Pfeiffer, "Ptychographic X-ray computed tomography at the nanoscale," *Nature* **467**, 436–439 (2010).
2. M. Holler, A. Diaz, M. Guizar-Sicairos, P. Karvinen, E. Färm, E. Härkönen, M. Ritala, A. Menzel, J. Raabe, and O. Bunk, "X-ray ptychographic computed tomography at 16 nm isotropic 3D resolution," *Sci. Rep.* **4**, 3857 (2014).
3. S. C. Mayo, A. W. Stevenson, and S. W. Wilkins, "In-Line Phase-Contrast X-ray Imaging and Tomography for Materials Science," *Materials* **5**, 937–965 (2012).

4. B. Chen, M. Guizar-Sicairos, G. Xiong, L. Shemilt, A. Diaz, J. Nutter, N. Burdet, S. Huo, J. Mancuso, A. Monteith, F. Vergeer, A. Burgess, and I. Robinson, "Three-dimensional structure analysis and percolation properties of a barrier marine coating," *Sci. Rep.* **3**, 1177 (2013).
5. K. Nugent, T. Gureyev, D. Cookson, D. Paganin, and Z. Barnea, "Quantitative Phase Imaging Using Hard X Rays," *Phys. Rev. Lett.* **77**, 2961–2964 (1996).
6. P. Cloetens, W. Ludwig, J. Baruchel, D. Van Dyck, J. Van Landuyt, J. P. Guigay, and M. Schlenker, "Holotomography: Quantitative phase tomography with micrometer resolution using hard synchrotron radiation x-rays," *Appl. Phys. Lett.* **75**, 2912–2914 (1999).
7. S. C. Mayo, P. R. Miller, S. W. Wilkins, T. J. Davis, D. Gao, T. E. Gureyev, D. Paganin, D. J. Parry, A. Pogany, and A. W. Stevenson, "Quantitative X-ray projection microscopy: phase-contrast and multi-spectral imaging," *J. Microsc.* **207**, 79–96 (2002).
8. R. Mokso, P. Cloetens, E. Maire, W. Ludwig, and J.-Y. Buffiere, "Nanoscale zoom tomography with hard x rays using Kirkpatrick-Baez optics," *Appl. Phys. Lett.* **90**, 144104 (2007).
9. J. Miao, P. Charalambous, and J. Kirz, "Extending the methodology of X-ray crystallography to allow imaging of micrometre-sized non-crystalline specimens," *Nature* **400**, 342–344 (1999).
10. J. M. Rodenburg, A. Hurst, A. Cullis, B. Dobson, F. Pfeiffer, O. Bunk, C. David, K. Jefimovs, and I. Johnson, "Hard-X-Ray Lensless Imaging of Extended Objects," *Phys. Rev. Lett.* **98**, 034801 (2007).
11. B. Abbey, K. A. Nugent, G. J. Williams, J. N. Clark, A. G. Peele, M. A. Pfeifer, M. de Jonge, and I. McNulty, "Keyhole coherent diffractive imaging," *Nat. Phys.* **4**, 394–398 (2008).
12. P. Thibault, M. Dierolf, A. Menzel, O. Bunk, C. David, and F. Pfeiffer, "High-resolution scanning x-ray diffraction microscopy," *Science* **321**, 379–82 (2008).
13. A. Schropp, R. Hoppe, J. Patommel, D. Samberg, F. Seiboth, S. Stephan, G. Wellenreuther, G. Falkenberg, and C. G. Schroer, "Hard x-ray scanning microscopy with coherent radiation: beyond the resolution of conventional x-ray microscopes," *Appl. Phys. Lett.* **100**, 253112 (2012).
14. M. Langer, P. Cloetens, J.-P. Guigay, and F. Peyrin, "Quantitative comparison of direct phase retrieval algorithms in in-line phase tomography," *Med. Phys.* **35**, 4556–4566 (2008).
15. J. Hagemann, D. R. Luke, C. Homann, T. Hohage, P. Cloetens, H. Suhonen, and T. Salditt, "Reconstruction of wave front and object for inline holography from a set of detection planes," *Opt. Express* **22**, 195–202 (2014).
16. C. Homann, T. Hohage, J. Hagemann, A.-L. Robisch and T. Salditt, "Validity of the empty-beam correction in near-field imaging," *Phys. Rev. A* **91**, 018321 (2015).
17. J. Villanova, J. Laurencin, P. Cloetens, P. Bleuët, G. Delette, H. Suhonen, and F. Usseglio-Viretta, "3D phase mapping of solid oxide fuel cell YSZ/Ni cermet at the nanoscale by holographic X-ray nanotomography," *J. Power Sources* **243**, 841–849 (2013).
18. M. Stockmar, P. Cloetens, I. Zanette, B. Enders, M. Dierolf, F. Pfeiffer, and P. Thibault, "Near-field ptychography: phase retrieval for inline holography using a structured illumination," *Sci. Rep.* **3**, 1927 (2013).
19. M. Stockmar, P. Cloetens, A. Bonnin, I. Zanette, M. Dierolf, B. Enders, R. Clare, F. Pfeiffer, and P. Thibault, "X-ray near-field ptychography for optically thick specimens," *Phys. Rev. Appl.* **3**, 014005 (2015).
20. A. Suzuki, S. Furutaku, K. Shimomura, K. Yamauchi, Y. Kohmura, T. Ishikawa, and Y. Takahashi, "High-Resolution Multislice X-Ray Ptychography of Extended Thick Objects," *Phys. Rev. Lett.* **112**, 053903 (2014).
21. D. Paganin, *Coherent X-Ray Optics (Oxford Series on Synchrotron Radiation)* (Oxford University, 2006).
22. J. Als-Nielsen and D. McMorrow, *Elements of Modern X-ray Physics* (Wiley, 2001).
23. A. C. Kak and M. Slaney, *Principles of Computerized Tomographic Imaging (Classics in Applied Mathematics)* (Society for Industrial Mathematics, 1987).
24. M. Born and E. Wolf, eds., *Principles of Optics: Electromagnetic Theory of Propagation, Interference and Diffraction of Light*, 7th ed. (Cambridge University, 1999).
25. G. Martínez-Criado, R. Tucoulou, P. Cloetens, P. Bleuët, S. Bohic, J. Cauzid, I. Kieffer, E. Kosior, S. Labouré, S. Petitgirard, A. Rack, J. A. Sans, J. Segura-Ruiz, H. Suhonen, J. Susini, and J. Villanova, "Status of the hard X-ray microprobe beamline ID22 of the European Synchrotron Radiation Facility," *J. Synchro. Rad.* **19**, 1–9 (2011).
26. W. H. Richardson, "Bayesian-Based Iterative Method of Image Restoration," *J. Opt. Soc. Am.* **62**, 55–59 (1972).
27. L. Lucy, "An iterative technique for the rectification of observed distributions," *Astronom J* **79**, 745–754 (1974).
28. P. Thibault, M. Dierolf, O. Bunk, A. Menzel, and F. Pfeiffer, "Probe retrieval in ptychographic coherent diffractive imaging," *Ultramicroscopy* **109**, 338–343 (2009).
29. P. Thibault and A. Menzel, "Reconstructing state mixtures from diffraction measurements," *Nature* **494**, 68–71 (2013).
30. P. Thibault and M. Guizar-Sicairos, "Maximum-likelihood refinement for coherent diffractive imaging," *New J. Phys.* **14**, 063004 (2012).
31. C. T. Putkunz, M. A. Pfeifer, A. G. Peele, G. J. Williams, H. M. Quiney, B. Abbey, K. A. Nugent and I. Nulty, "Fresnel coherent diffraction tomography," *Opt. Express* **18**, 11746–11753 (2010).
32. P. Perona and J. Malik, "Scale-space and edge detection using anisotropic diffusion," *IEEE Trans. Pattern Anal. Mach. Intel.* **12**, 629–639 (1990).
33. N. Otsu, "A Threshold Selection Method from Gray-Level Histograms," *IEEE Trans. Syst., Man, Cybernet.*

- 62–66 (1979).
34. J. Laurencin, R. Quey, G. Delette, H. Suhonen, P. Cloetens, and P. Bleuet, “Characterisation of Solid Oxide Fuel Cell Ni₈YSZ substrate by synchrotron X-ray nano-tomography: from 3D reconstruction to microstructure quantification,” *J. Power Sources* **198**, 182–189 (2012).
 35. F. Usseglio-Viretta, J. Laurencin, G. Delette, J. Villanova, P. Cloetens, and D. Leguillon, “Quantitative microstructure characterization of a Ni-YSZ bi-layer coupled with simulated electrode polarisation,” *J. Power Sources* **256**, 394–403 (2014).
 36. G. Delette, J. Laurencin, F. Usseglio-Viretta, J. Villanova, P. Bleuet, E. Lay-Grindler, and T. Le Bihan, “Thermoelastic properties of SOFC/SOEC electrode materials determined from three-dimensional microstructural reconstructions,” *Int. J. Hydro. Energy* **38**, 12379–12391 (2013).
 37. T. Kanit, S. Forest, I. Galliet, V. Mounoury, and D. Jeulin, “Determination of the size of the representative volume element for random composites: statistical and numerical approach,” *I. J. Sol. Struct.* **40**, 3647–3679 (2003).
 38. B. Enders, M. Dierolf, M. Stockmar, F. Pfeiffer, and P. Thibault, “Ptychography with broad-bandwidth radiation,” *Appl. Phys. Lett.* **104**, 171104 (2014).
 39. M. van Heel and M. Schatz, “Fourier shell correlation threshold criteria,” *J. Struct. Biol.* **151**, 250–262 (2005).
 40. A. Ruhlandt, M. Krenkel, M. Bartels, and T. Salditt, “Three-dimensional phase retrieval in propagation-based phase-contrast imaging,” *Phys. Rev. A* **89**, 033847 (2014).
 41. A. Maiden, M. Humphry, and J. Rodenburg, “Ptychographic transmission microscopy in three dimensions using a multi-slice approach,” *J. Opt. Soc. Am. A* **29**, 1606–1614 (2012).
-

1. Introduction

X-ray micro- or nano-computed tomography provides high-resolution access to a sample’s internal structure in a non-destructive way [1, 2]. It is especially powerful in materials science research since the performance of novel functional materials is strongly determined by their structure on the micrometer or nanometer scale [3, 4].

To obtain a tomographic dataset with both high spatial resolution and high density sensitivity, propagation-based imaging or inline holography can be used [5, 6, 7]. Being a lensless technique, limitations of x-ray optics are circumvented thanks to an a posteriori phase retrieval step. When implemented in a cone beam magnification [8], propagation based imaging can be performed on a variety of different length scales and bridges the gap to coherent diffractive imaging (CDI) methods [9, 10, 11, 12, 13]. Unlike the latter, propagation-based imaging is based on near-field diffraction i.e. short propagation distances rather than far-field diffraction and thus benefits from lower requirements to the beam’s coherence and the detector’s dynamic range.

However, the phase retrieval step in propagation imaging needed prior to tomographic reconstruction remains challenging when the investigated sample is strongly absorbing and refracting, i.e. when linearization of the transmission function is no longer a valid approximation: Difficulties arise when phase retrieval is based on a linear model [14]. Additional artifacts can occur when the recorded diffraction patterns are normalized with a flat-field to correct inhomogeneities in the incident illumination. This procedure does not account for the co-propagation of inhomogeneities in the incident illumination with the waves diffracted by the sample, yielding reconstruction artifacts mainly at high resolutions [8, 15, 16].

For multiple samples of interest, including new materials for energy conversion, e.g. fuel cells, such strongly absorbing and phase shifting specimen cannot be avoided. Previous experiments which studied the microstructure of solid oxide fuel cells (SOFC) electrodes were carried out at high energy to reduce absorption and phase shift. Additionally, a priori knowledge about this sample’s chemical composition and assumptions on the sample’s homogeneity were used for phase retrieval [17].

Near-field ptychography [18] was recently applied successfully at a conventional inline holography setup to perform phase retrieval on an optically thick sample without requiring any prior knowledge about the sample [19]. Since near-field ptychography inherently incorporates the wave nature of x-rays and reconstructs the illumination function along with the

sample's transmission function, the aforementioned issues with flat-field normalization are circumvented as well. In this work, ptychographic reconstructions of a sequence of projections of the sample are combined to form a local tomographic dataset which is then tomographically reconstructed. The sample investigated consists of a part of different layers of a solid-state oxide fuel cell (SOFC). Morphological features are extracted and compared to results obtained with holotomography [6, 17]. We show that near-field ptychographic local x-ray nano CT can be a valuable and robust tool to access the three-dimensional nano structure of a sample and will be especially useful for strongly absorbing and phase shifting materials.

2. Fundamentals

2.1. Interaction of the sample with the x-ray beam

In the following, we assume that sample is illuminated by a monochromatic x-ray wave with a wavelength of λ . If diffraction effects inside the sample can be neglected i.e. the maximum sample thickness t_{max} obeys

$$t_{max} \leq r^2/\lambda, \quad (1)$$

where r is the resolution of the imaging system, the projection approximation can be used [20]. In this case, the interaction of the sample with the x-ray beam can be described by the sample transmission function $T(x,y)$, which represents a two-dimensional projection of the three-dimensional distribution of the complex index of refraction [21] n :

$$T(x,y) = A(x,y) \exp[i\phi(x,y)] = \exp[-k \int \beta(x,y,z) dz] \cdot \exp[-ik \int \delta(x,y,z) dz], \quad (2)$$

where

$$n(x,y,z) = 1 - \delta(x,y,z) + i\beta(x,y,z). \quad (3)$$

The imaginary part $\beta(x,y,z)$ is related to photoelectric absorption of x-rays and affects the amplitude $A(x,y)$ of the sample transmission function, while the phase $\phi(x,y)$ of $T(x,y)$ is determined by the refractive index decrement $\delta(x,y,z)$ which is related directly to the electron density $\rho(x,y,z)$ via $\delta(x,y,z) = \frac{2\pi r_0 \rho(x,y,z)}{k^2}$ where $k = \frac{2\pi}{\lambda}$ and $r_0 = 2.817940 \text{ fm}$ denotes the classical electron radius [22].

The three-dimensional distribution of $\delta(x,y,z)$ and $\beta(x,y,z)$ can be accessed via tomographic reconstruction techniques [23], which require that the sample is rotated around the vertical axis and the transmission function is determined for a sufficient number of projection angles. The set of the transmission functions for the different angles can be stacked to a three-dimensional array. A two-dimensional slice through this array perpendicular to the rotation axis is called a sinogram.

2.2. Inline holography and phase retrieval

In a generic inline holographic setup, a diffraction pattern $I(x,y)$ or hologram of the sample is recorded on a pixelated detector. To obtain effective pixel sizes Δx much smaller than the physical pixel size Δs of the detector, a cone beam illumination can be used to acquire a magnified hologram of the sample's exit wave $\chi(x,y)$. The magnification M is given by

$$M = \frac{z_1 + z_2}{z_1}, \quad (4)$$

where z_1 corresponds to the focal point-sample distance and z_2 to the sample-detector distance, resulting in a smaller effective pixel size of $\Delta x = \Delta s/M$, where Δs denotes the physical pixel size

of the detector. The diffracted intensities can be described by the angular-spectrum formulation of Fresnel diffraction

$$I(x, y) = |D_{z_{\text{eff}}}[\chi(x, y)]|^2 = |F^{-1}[F[\chi(x, y)] \cdot \exp(i\Delta z_{\text{eff}}\sqrt{k^2 - q_x^2 - q_y^2})]|^2, \quad (5)$$

where F denotes the Fourier transform with reciprocal coordinate q , $k = 2\pi/\lambda$ the wavenumber, and $z_{\text{eff}} = z_2/M$ the effective propagation distance corresponding to a parallel beam wavefront [21].

Since the phases of the wavefield are lost and only the intensities $I(x, y)$ can be measured, we have only $N_x N_y$ constraints corresponding to the number of pixel on the detector but $2N_x N_y$ unknowns. To retrieve the phases, additional constraints need to be introduced or additional measurements need to be carried out.

In holotomography, measurement diversity is created by recording the diffracted intensities at several different sample-detector distances (often 4 distances) which allows the use of a phase-retrieval scheme to retrieve the sample's transmission function $T(x, y)$. To obtain a tomographic dataset, the sample is rotated and the procedure is repeated for a given number of rotation angles.

In near-field ptychography, multiple intensity measurements

$$I_j(x, y) = |D_{z_{\text{eff}}}[\chi_j(x, y)]|^2 \quad (6)$$

are carried out at the same propagation distance z_{eff} but for different relative positions $\vec{r}_j = (x_j, y_j)$ of the sample $T(x, y)$ perpendicular to the incoming illumination ψ . The exit waves are then described by

$$\chi_j(x, y) = \psi(x, y)T(x - x_j, y - y_j). \quad (7)$$

To produce measurement diversity in the different diffraction patterns, the incident wavefront needs to deviate sufficiently from a uniform illumination. If the sample were scanned with respect to uniform illumination, the diffraction patterns would be identical except for a lateral shift (and boundary effects) so that no measurement diversity would be created. Sufficient deviation from a uniform illumination can be achieved, e.g. by placing a static random phase screen upstream of the sample. In far-field ptychography, enough translational measurement diversity is typically created if the illumination is locally confined i.e. the sample is larger than the field-of-view (FOV). In near-field geometry, however, even in this case, the illumination has to be sufficiently structured, as diffraction is significant only within a few times the width of a Fresnel zone [24], which is usually much smaller than the FOV. If a set of diffraction patterns $I_j(x, y)$ with different relative positions \vec{r}_j of the sample with respect to the beam has been acquired, different ptychographic phase retrieval algorithms can be used to retrieve the sample transmission function $T(x, y)$ along with the illumination function $\psi(x, y)$. Further details on near-field ptychography can be found in literature [18].

To obtain a tomographic dataset, the ptychographic scan and reconstruction needs to be repeated sequentially for a sufficient number of projection angles.

3. Methods and materials

3.1. Sample

The sample, cut from of a commercially available SOFC to a maximum thickness of $t_{\text{max}} \approx 125\mu\text{m}$, was also investigated in previous experiments using holotomography [17]. The fuel cell contains four different layers: The top layer consists of the current collector which is made of Lanthanum Strontium Manganite (LSM). The second layer comprises the cathode made of microporous LSM and Ytria stabilised Zirconia (YSZ) and is followed by the third, dense

YSZ electrolyte layer. The bottom part consists of a microporous anode which is composed of Nickel and YSZ. The anode is further divided into a thin anode functional layer (AFL) where the electrochemical reactions take place and which contains a finer microstructure. The second part of the anode is made up of the support structure which is responsible for the gas exchange and features a coarser microstructure.

3.2. Experimental setup

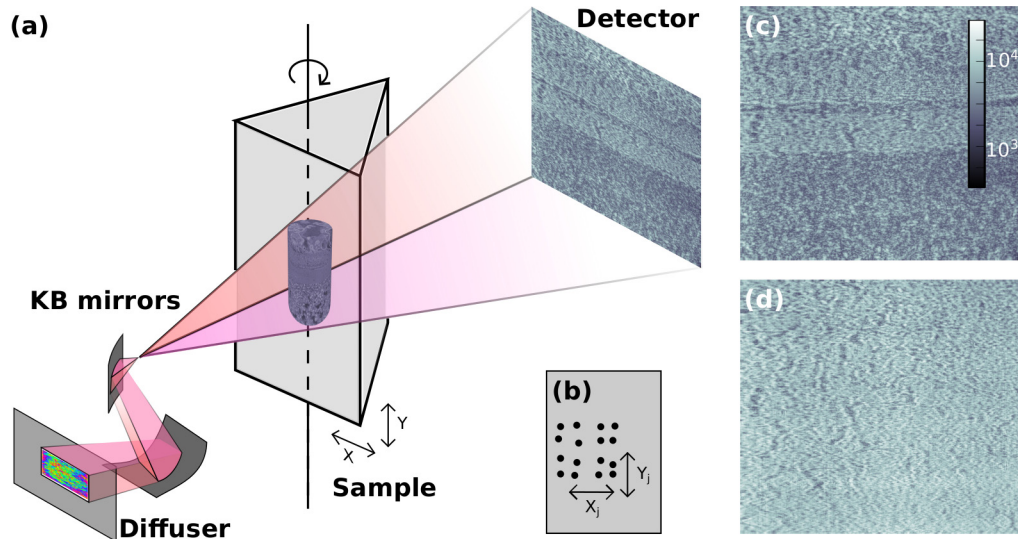


Fig. 1. (a) Schematics of the setup used. (b) Scanning pattern. (c) One diffraction pattern of the sample. (d) Diffraction pattern of the beam without the sample.

The experiments were carried out at the nano-imaging endstation of beamline ID22 at the European Synchrotron Radiation Facility (ESRF), Grenoble, France [25]. This endstation was used for holotomography experiments on a regular basis. Schematics of the setup are shown in Fig. 1. The primary x-ray source consists of an undulator located 64 m upstream of a pair of crossed Kirkpatrick-Baez (KB) mirrors which produce a virtual secondary source with a full width half maximum of about 80 nm. The mean energy was $E = 16.9$ keV with a bandwidth of about 2%. A lens-coupled scintillator-based FReLoN camera with 2048^2 pixels with a pixel size of $0.756 \mu\text{m}$ and 14 bit dynamic range and is located at a distance $z_1 + z_2 = 52.525$ cm downstream of the focal point of the KB mirror. The sample was placed at a distance of $z_1 = 1.87$ cm past the focus resulting in a magnification of $M = 30.5$, an effective pixel size $\Delta x = 24.8$ nm and an effective propagation distance of $z_{\text{eff}} = 1.67$ cm. The field of view (FOV) at that position is about $w = 50.7 \mu\text{m}$. To structure the illuminating wavefront, a static diffuser consisting of a piece of cardboard was mounted in front of the KB mirrors.

The tomographic scan consisted of 1200 angles regularly distributed over an angular range of 180° where at each angular position a ptychographic scan was acquired. A single ptychographic scan comprised 16 pseudo-randomly distributed points with a maximum shift of 350 pixels. At each point a diffraction pattern was acquired using an exposure time of 0.5 s. After every 10 ptychographic scans, an image of the beam without sample was acquired.

3.3. Ptychographic reconstruction

The path from the diffraction data to the 3D volume consisted of three main steps: pre-processing of the diffraction data, ptychographic reconstruction of the projected transmission function $T(x,y)$ for every angle θ , and tomographic reconstruction to obtain the 3D distribution. In a subsequent fourth step described in the second-next subsection, the microstructural properties of the anode were analyzed.

In the pre-processing step, the diffraction patterns were corrected for dark current and rebinned by a factor of two yielding diffraction patterns with 1024^2 pixels and an effective pixel size of $\Delta x = 49.6$ nm. With these corrections, ptychographic reconstruction was already successful and of high quality. But due to the ready availability of the detector point-spread-function characterization from past experiments at the beamline (and standard procedure for inline-holographic experiments), a deconvolution using 5 iterations of the Richardson-Lucy-algorithm [26, 27] was carried out on the diffraction patterns resulting in slightly improved reconstructions.

First, the ptychographic reconstruction was carried out for the angle $\theta = 0^\circ$ using 1000 iterations of the difference map (DM) algorithm [28]. The result was further improved in a refinement step by adding two additional modes to the illumination function [29] and employing 330 iterations of the DM algorithm and 500 iterations of the maximum likelihood (ML) algorithm [30]. The additional modes add additional degrees of freedom to the reconstruction. They can pick up illumination characteristics and general inconsistencies between the measured data and the forward model (Eq. 6) used for reconstruction. The output of this refinement step then served as initial guess for the reconstruction of the next neighboring angle which could be started with the refinement step. This procedure was used in Fresnel coherent diffraction tomography before and was termed the “bootstrap” method [31]. Projections of neighboring angles were sufficiently similar for this strategy to apply to the second next angles, thereby doubling the number of parallel reconstruction processes. As in a previous experiment [19], the additionally recorded images of the beam without sample were used to further suppress raster-grid artifacts and to support the reconstruction of the illumination function, but not to normalize the diffraction patterns. The focal spot size of the KB mirrors determines the best achievable spatial resolution in this setup. With the given maximum thickness of the sample, the projection approximation is at the edge of validity (Eq. 1) since $\sqrt{\lambda t_{max}} \approx 96$ nm $\leq 2\Delta x$. A thicker sample would further degrade the resolution.

The 2% bandwidth of the radiation results in a 1% difference in fringe spacing, given by $\sqrt{\lambda_{z_{eff}}}$, and corresponds to less than a quarter of a pixel. Consequently, polychromatic propagation is negligible in this case and the regular monochromatic forward model (Eq. 6) was used.

3.4. Tomographic reconstruction

The tomographic reconstruction was performed only on the sinograms obtained from the phase images of reconstructed sample transmission functions. Regions close to the border where the ptychographic reconstruction is less constrained were cropped out. A region with 240 pixels width was additionally cropped to center the axis of rotation. To circumvent phase unwrapping, the sinogram was differentiated in the direction orthogonal to the rotational axis and filtered back projection (FPB) was carried out using a Hilbert filter [23]. The final size of the reconstructed volume was $872^2 \times 1098$ voxels corresponding to a volume of $43.2 \mu\text{m}^2 \times 54.4 \mu\text{m}$.

3.5. Analysis of the microstructural properties

The analysis procedure to obtain microstructural properties of the anode from the reconstructed volume is described in detail elsewhere [17] and is only briefly summarized hereafter. Image

processing is preliminarily carried out on the 3D reconstruction. As a first step, anisotropic diffusion filtering [32] is applied to the volume to flatten the grey levels within the phases and enhances the contrast at the boundaries [17]. In the second step, the volume is segmented by finding the thresholds between each peak of the grey level distribution. For this, the method proposed by Otsu [33] has been implemented in Matlab. It provides fully automated processing based on a statistical treatment of the grey level distribution. A criterion that indicates the quality of the thresholding is also calculated at the end of the numerical processing. This criterion varies between 0 and 1, where a value of 1 indicates an ideal segmentation. After these two processing steps, the 3D microstructure can be analyzed with the methods already presented in literature [34, 35]. Volume fractions and density of Triple-Phase Boundary Lengths (TPBL) were directly computed on the whole reconstructed volume. Unlike volume fraction and TPBL, specific surface areas and mean particle diameters are deduced from the covariance function [35]. This mathematical function, which provides a morphological indicator of the heterogeneous microstructure, represents the probability that two points separated by a distance h belong to the same phase. They were computed for each phase of the electrode on several independent subvolumes extracted from the whole reconstruction. Nine subvolumes of $10\mu\text{m} \times 10\mu\text{m} \times 10\mu\text{m}$ were investigated for the reconstructed AFL, while four subvolumes of $15\mu\text{m} \times 15\mu\text{m} \times 15\mu\text{m}$ were used for the substrate. These subvolumes were considered as stochastic volume elements (SVE) [36, 37] so that properties were averaged from these several realizations.

4. Results and discussion

4.1. Projections reconstructed by ptychography

The result of the ptychographic reconstruction is shown for a single projection angle in Fig. 2. The phase of the reconstructed transmission function shows strong modulations and allows clear separation of the four layers of the SOFC. The amplitude image features high absorption but also artifacts and a noisier appearance. Due to the latter two, the FBP of the absorption part gave only poor results. The reconstructed probe looks similar to those obtained in previous experiments at the same setup using the same diffuser [18, 19]. The main modes took up 70% of the the total power, the two additional modes each took up 15% of the power. Since the illumination does not decrease to zero at the borders of the FOV and the sample greatly extends outside the FOV, the edges of the diffraction pattern are not consistent with our propagation model. The additional modes account for those inconsistencies, as they do with far-field ptychography [38].

The spatial resolution of the 2D phase projections was estimated by calculating the Fourier ring correlation (FRC) [39] of two neighboring projections. The 0.5 threshold of the FRC corresponds to a resolution of about 121 nm.

4.2. Reconstructed volume

Figure 3 shows different slices through the volume reconstructed from the projections of the phase image. In the transverse slice, the four different layers consisting of cathode current collector, cathode functional layer, electrolyte and anode (from top to bottom) are clearly visible. The contrast in the anode is sufficient to distinguish between the three different phases which are present in the material: the dark areas correspond to porosities, the grey voxels correspond to the ceramic phase consisting of YSZ and the brightest voxels belong to the metallic Ni phase. Upon visual inspection, the reconstructed volume is in good agreement with the reconstructions obtained with holotomography on the same sample [17]. A comparison of the anode layer obtained with both methods is done in the next subsection.

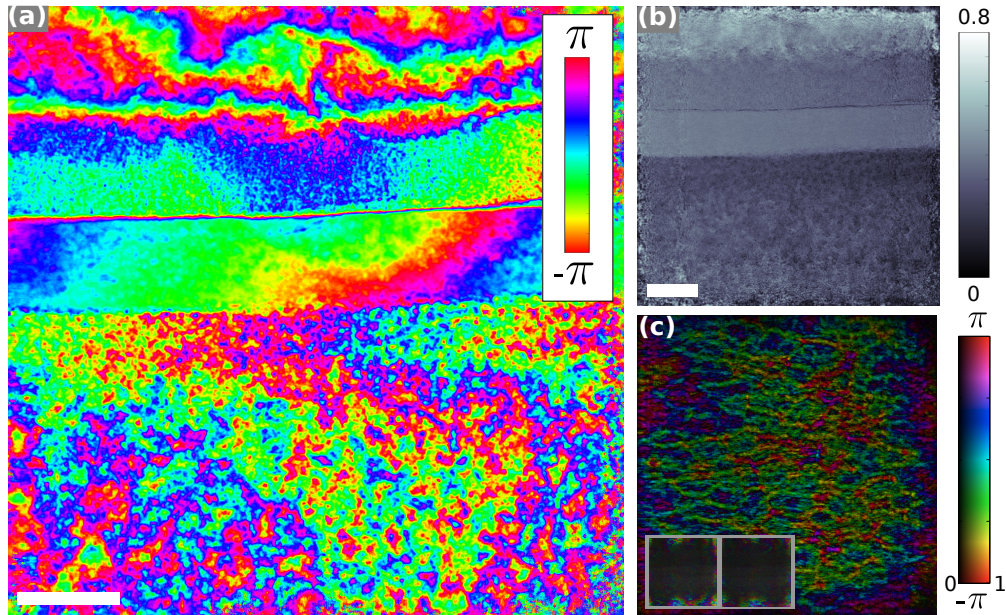


Fig. 2. Ptychographic reconstruction results for a single projection angle. (a) Wrapped phase of the sample transmission function. (b) Magnitude of the sample transmission function. (c) Main mode of the complex valued illumination function with additional modes as insets. The scale bars indicate 10 μm .

To estimate the resolution of the reconstructed volume, the set of projections was split into the projections with even and the projections with odd numbers. This allowed the reconstruction of two different volumes. The 0.5 threshold of the Fourier shell correlation [39] of those two volume yields 125 nm as an estimate for the spatial resolution in 3D.

4.3. Comparison to holotomography and extracted microstructural properties

Figs. 4(a) and 4(c) provide 2D images extracted from the 3D reconstructed cell support (anode substrate) obtained by near-field ptychographic CT before and after segmentation. These images are compared to the ones previously obtained on the same sample at the same setup (without diffuser) by holotomography at 29 keV (and a voxel size of 25 nm) [17] (Figs. 4(b) and 4(d)). Upon direct visual inspection, the reconstructed images show similar qualities and seem to exhibit the same microstructural features. It is worth emphasizing that good phase separation criteria have been computed on the volume obtained from the ptychographic reconstructions. The values are equal to 0.916 for the AFL and 0.896 for the substrate, and lie in the same range as the ones obtained from the holotomographic volumes (0.904 for the AFL and 0.912 for the substrate [17]). In other words, the 3D ptychographic raw images feature the same quality as the holotomographic ones and exhibit a grey level distribution that allows a very good phase thresholding. The covariance functions of the ptychographic reconstruction are plotted in Fig. 4(e) for the AFL and compared to the ones calculated with the holotomographic volume [35]. It can be noticed that the curves for the solid phases are quasi identical, whereas a slight difference is visible for the porosity. Nevertheless, it can be inferred from this comparison that the two types of reconstructions exhibit the same morphological features. In addition, microstructural parameters have also been calculated for the AFL and the substrate. The results are provided in Table 1 and compared to the ones obtained with holotomography. The two sets of microstructural prop-

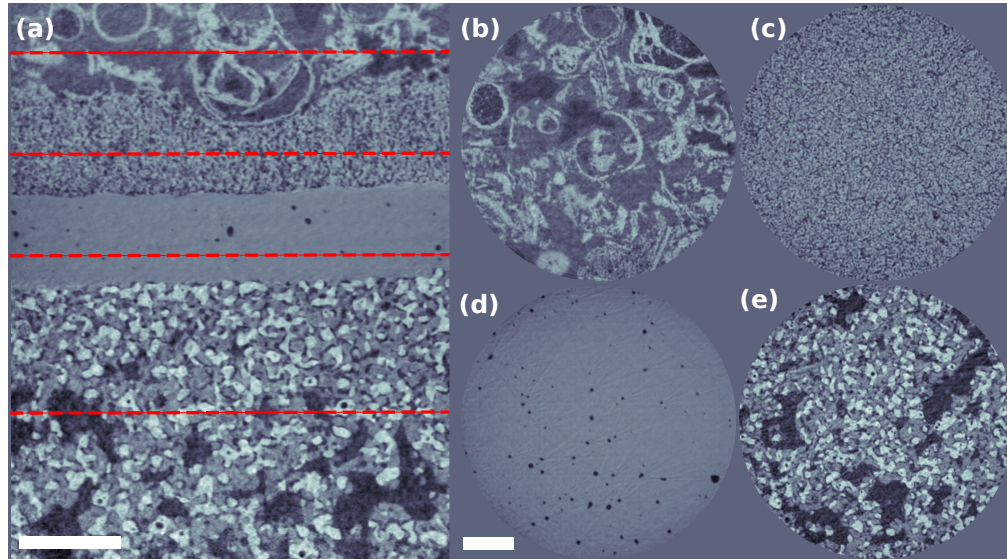


Fig. 3. Tomographic reconstruction results: (a) Frontal slice through the center. Transverse slices depicting (b) the cathode current collector, (c) the cathode functional layer, (d) the electrolyte and (e) the anode substrate. The scale bars indicate 10 μm .

erties are in good agreement even though a slight deviation can be noticed for the substrate. Indeed, for the substrate, the differences can be explained by a difference in analyzed volumes. For holotomography, the properties have been computed on a reconstruction whose dimensions are equal to the Representative Volume Element (RVE) (i.e. $35 \mu\text{m} \times 35 \mu\text{m} \times 35 \mu\text{m}$ [34]). Conversely, for near-field ptychographic CT, the properties have been calculated on a smaller volume equivalent to a cubic volume of $25.8 \mu\text{m} \times 25.8 \mu\text{m} \times 25.8 \mu\text{m}$. In that condition, it can be noticed that the results obtained with the near-field ptychographic volume lie in the standard deviation of the properties when several realizations of this volume are used.

5. Summary and outlook

In this paper, we have demonstrated that near-field ptychographic phase retrieval can be used to obtain a tomographic dataset for local nano CT of a strongly absorbing and phase shifting sample, giving access to a much broader range of possible samples.

From a sample's perspective, near-field ptychography might be suitable in all instances where holotomography would be the method of choice, but where difficulties from strong absorption and phase shift or strong inhomogeneities in the illumination arise, or where prior knowledge of the sample needs be used for phase retrieval. Therefore, we have compared the results obtained with near-field ptychographic CT with the results obtained with holotomography from a previous experiment. Upon visual inspection, the obtained images are of similar quality. To quantify this, microstructural properties of the anode were compared for both modalities and are in good agreement within statistical errors. Holotomography was carried out at an energy of 29 keV since the reconstruction of the data obtained at 16.9 keV did not yield usable results for this specific sample. Moreover, holotomography required some a priori knowledge about the sample to perform phase retrieval. Compared to far-field ptychography, near-field ptychography (in combination with a cone beam geometry) might be more efficient for larger specimens which would require many scanning points in far-field ptychography.

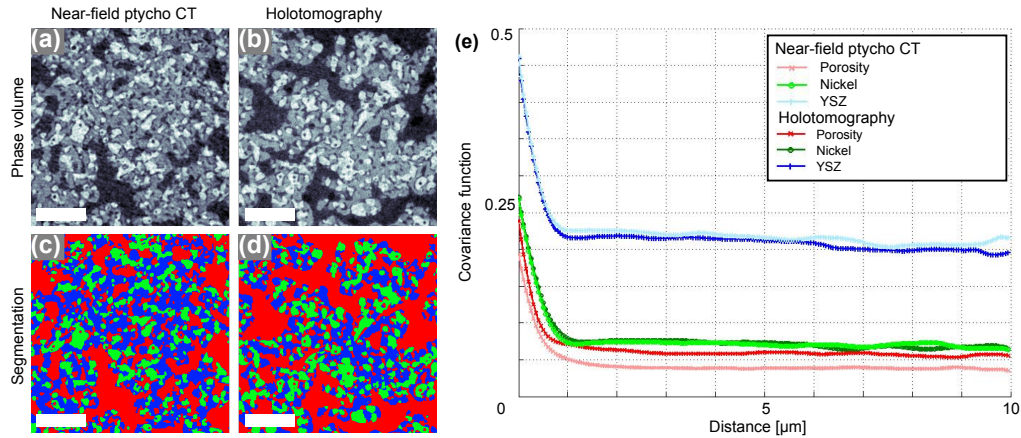


Fig. 4. Analysis of the anode substrate microstructure and comparison with holotomography. (a) shows a slice of the volume obtained by near-field ptychography, (c) shows the same slice after segmentation into the gas phase (red), the ceramic phase (blue) and the metallic phase (green). A similar slice (but not the same slice) of the volume obtained by holotomography is shown before (b) and after segmentation (d). The scale bars indicate 5 μm . (e) A plot comparing the covariance functions for each phase obtained from the segmentation of the near-field ptychography CT volume (faint colors) and the volume obtained by holotomography (bright colors).

Table 1. Comparison of the anodes's microstructural properties. Rel. Dev. denotes the relative deviation of the values obtained with near-field ptychographic (NFP) CT with respect to the value obtained with holotomography.

	AFL		Rel. Dev. [%]	Anode substrate		
	Holotomo.	NFP CT		Holotomo.	NFP CT	Rel. Dev. [%]
Volume fraction [%]						
Porosity	22.8	22.6	1	46.6	39.6	15
YSZ	5.50	5.01	9	6.01	5.12	15
Ni	28.2	27.2	2	21.7	23.8	10
Specific surface area [μm^2]						
Porosity	9.09	7.82	14	4.24	5.37	27
YSZ	5.50	5.01	9	6.01	5.12	15
Ni	6.54	6.44	2	5.87	6.45	10
Mean particle diameter [μm]						
Porosity	0.94	0.97	3	2.6	2.25	10
YSZ	0.72	0.82	13	1.1	1.1	0
Ni	0.83	0.93	12	1.2	1.2	0
TPBL [$\mu\text{m} / \mu\text{m}^3$]						
Global	4.63	5.64	22	3.46	5.76	66
Active	3.30	2.78	16	2.61	2.92	12

Future algorithmic development of near-field ptychography should allow extraction of a usable amplitude signal to provide additional and complimentary information. Moreover, algorithmic development should focus on exploiting the redundancies due to the tomographic acquisition to further reduce the required data, which in this case was four times the amount

collected for holotomography. This reduction would reduce the duration of both acquisition and reconstruction, which at the moment still takes significantly more time than in holotomography. By using iterative tomographic reconstruction techniques instead of FBP the number of angular samples and therefore the total number of diffraction patterns might be further reduced. The ultimate goal would be to combine near-field ptychographic phase-retrieval and tomographic reconstruction in a single reconstruction scheme as was already done for hybrid-input-output based holographic phase retrieval [40]. However, current developments in the field of ptychographic reconstruction software, in particular the use of graphical processor units (GPUs) for massively parallel computing, are expected to further boost the speed of ptychographic phase retrieval.

As indicated earlier, the projection approximation was at the edge of validity in this experiment. For future local CT experiments carried out with thicker samples or at higher resolutions, the adaption of existing multi-slice reconstruction techniques [41, 20] for near-field ptychography might be necessary. Finally, the effects of polychromaticity on near-field ptychography and possibilities to refine the forward model to include such effects should be carried out in future work. This might even allow to translate near-field ptychography to less monochromatic sources.

Acknowledgments

We acknowledge financial support through the DFG Cluster of Excellence Munich-Centre for Advanced Photonics (MAP), the DFG Gottfried Wilhelm Leibniz program, the European Research Council (ERC, starting grant OptImaX) and the TUM Graduate School. Moreover, this work was supported by the German Research Foundation (DFG) and the Technische Universität München within the funding program Open Access Publishing.